university of groningen

faculty of science and engineering

BACHELOR THESIS ASTRONOMY

ANALYSIS OF X-RAY BURSTS AND MILLIHERTZ QUASI-PERIODIC OSCILLATIONS IN 4U 1636-53

Author: Oscar Greenwell
o.h.greenwell@student.rug.nl
Kapteyn Astronomical Institute
Supervisor:
Prof. Dr. R.M. (Mariano) Méndez

July 2018

Abstract

I investigated the spectral properties of millihertz quasi-periodic oscillations (mHz QPOs) in the neutron star low-mass X-ray binary (NS LMXB) system 4U 1636-53 using observations taken by the Rossi X-ray Timing Explorer (RXTE). The analysis of all X-ray bursts from this source show that all the type 1 X-ray bursts that were associated with a mHz QPO had a short rising time, were energetic, and also had a short duration. Kolmogorov-Smirnov testing showed to a high degree of certainty that X-ray bursts associated with a mHz QPO are from a different parent population than X-ray bursts that are not associated with a mHz QPO. The features of the X-ray bursts associated with a mHz QPO suggest a link between mHz QPOs and helium rich X-ray bursts. It was also found that in all 39 cases that a mHz QPO was associated to an X-ray burst, the burst had positive convexity. Kolmogorov-Smirnov testing showed to a high degree of certainty that this was not an anomalous result. According to recent models, convexity is related to the ignition site of an X-ray burst on the neutron star surface. My research suggests that in 4U 1636-53 the 39 bursts associated with a mHz QPO, and the marginally stable nuclear burning process responsible for their generation, both happen at the equator of the neutron star. This finding reconciles the disparity between the necessary high mass accretion rate needed to trigger mHz QPOs in theoretical models and the low mass accretion rate that is derived from observations.

Contents

1. Introduction

1.a. X-ray binaries

A large amount of stars in our universe are born into multiple star systems (Duchne & Kraus 2013); a binary star system is one such system that contains two stars that orbit around their common centre of mass. X-ray binaries are a further subset of binary star systems that consist of a main sequence star and a compact, dense star or object (a neutron star, white dwarf, or black hole). In the X-ray regime of the EM spectrum, X-ray binaries are some of the most luminous extra-solar objects in the sky [5][22]. They are characterised by pronounced variabilities in brightness which can occur on timescales ranging from mere milliseconds to days, months, and even years [22]. The source that fuels the tremendous power output of these systems is simply the gravitational energy released by matter that is stripped away from the companion star, which then accretes around the compact object in the system; in fact, the compact object in these binary systems is often termed the 'Accretor', and the companion star the 'Donor'.

There are two canonical forms of X-ray binaries; the HMXB (High Mass X-ray Binary) and the LMXB (Low Mass X-ray Binary), the classification of an X-ray binary system into either of these groups depends on the mass of the companion star in the system; if the mass of the companion star is above or below approximately two solar masses, it is considered an HMXB, or an LMXB, respectively (Zhang et al. 2012). In both of these cases the exact identity (neutron star, white dwarf, or black hole) of the co-orbiting compact object is not relevant vis-a-vis its classification. An HMXB is generally very active in the X-ray regime, and its companion star is often of the class O, B, Be, or even a blue supergiant (Zhang et al. 2012). The donor in an HMXB system produces powerful stellar winds, these winds assist in the accretion of large amounts of matter from the donor onto the accretor. In an LMXB system the donor is generally a low-mass main sequence star, and the accretion of matter from this star onto the accretor is driven predominantly by Roche lobe overflow. The system being studied in this thesis, 4U 1636-53, is one such LMXB system, composed of a neutron star and a low-mass main sequence star. In LMXB systems the transfer of mass occurs much slower than in an HMXB system. As the matter falls onto the star the law of conservation of angular momentum must be observed, and thus the matter cannot fall directly onto the compact object, the matter instead spirals into the object, forming a disk around it that is termed the 'accretion disk'. In the accretion disk, friction converts the kinetic energy of the in-falling matter into radiation, which is mainly observable in the X-ray band [22].

1.b. Neutron stars

A neutron star is one of the possible endpoints in the evolution of a high mass star. In simple terms, a neutron star is the collapsed core of a large star, which before collapse had a total mass of between 10 and 29 solar masses [18]. At higher masses the degeneracy pressure of the neutrons would not be able to counteract the forces of gravity and the core would collapse under its own gravity to form a black hole [18]. Neutron stars are the smallest and most dense form of stars that exist. In contrast with regular stars, neutron stars do not generate heat by means of fusion of reactants (or by other thermonuclear reactions) in their core [18]. A neutron star is composed of several layers: A thin atmosphere, a metal-poor ocean, a metal-rich solid crust and a core, made up almost entirely of neutrons, this core makes up the bulk of the star's mass [18]. The mass of a neutron star is around 1.4 solar masses [18], however, the radius of the star measures between 10-20 km across [18]. The density of the core can reach up to 10^{15}gm cm^3 [18].
Neutron stars were first proposed to exist in 1933 by Baade & Zwicky (1934); they suggested that a supernova explosion was the result of a main sequence star transitioning to a neutron star. Further work on a theoretical model for a neutron star was undertaken by Robert Oppenheimer and George Volkoff, who solved the general relativistic stellar structure equation for the case of a pure neutron gas, this yielded insight into the theoretical interior of a neutron star. It was not until 1967 that the first neutron star was discovered by Jocelyn Bell, however, to date, there have

been over a thousand known neutron stars verified through observation [18].

1.c. Thermonuclear bursts

During the accretion process in neutron star LMXBs, the accreted matter burns on the surface of the neutron star. There are two canonical modes of nuclear burning that occur on the neutron star surface, these are termed stable and unstable burning. During stable nuclear burning the surface of the neutron star emits thermally, whereas unstable burning is detected as a thermonuclear burst [28]. Thermonuclear bursts, also known as type-I X-ray Bursts, X-ray bursts, or simply, bursts, occur due to unstable burning of hydrogen and helium on the surface of accretors in LMXB systems. During these bursts the X-ray flux of the LMXB increases by a scale of ten to a hundred times its stable emission level (Zhang et al. 2012). These bursts occur within a timescale of a second or less, and the emission level drops back down within a tens of seconds (e.g. Galloway et al. 2008). The predominant shape of these X-ray bursts is characterised by a single-peaked, fast rising and exponentially decaying light curve, however type 1 X-ray bursts can show a variety of profiles, with some possessing double or multiple peaks (Lyu et al. 2016). In this thesis I will be analysing X-ray bursts from the neutron star LMXB object 4U 1636-53.

1.d. Burst properties

A burst possesses certain measurable quantities, the ones pertinent to this thesis are as follows:

1.d.1. Flux

Flux is the defined as the amount of energy emitted per unit time, per unit area by a source. In this thesis it is measured in the CGS units of erg cm^{-2} s^{-1}. The peak flux of a burst F_{peak} is the highest value of flux observed during a burst. For a black-body radiator, or a body being approximated as one, the flux received is equal to:

$$F_b = \frac{\sigma T_b^4 R^2}{d^2}, \tag{1}$$

where F_b represents the Flux received from a black body if it possesses a surface temperature T_b, and σ represents the Stefan-Boltzmann constant. R represents the radius of the emitting source, and d is the distance to the source.

1.d.2. Convexity

For bursts, such as those in figure 1, the convexity is a dimensionless quantity which relates to how convex (positive convexity) or concave (negative convexity) the profile of the rising part of the burst is. Convexity thus gives us insight into the shape of the rising part of a burst's light curve. it is defined as the integrated area of the burst light curve above (in the case of positive convexity) or below (negative convexity) a straight line drawn from the start of the burst to the peak of the burst (see figure 1). A burst with 0 convexity is therefore observed as having a rising profile that is a straight line. It was posited in recent theoretical work (Maurer and Watts 2008; Mahmoodifar and Strohmayer 2015) that the convexity of type 1 X-ray bursts is related directly to the latitude on the neutron star where the bursts ignite.

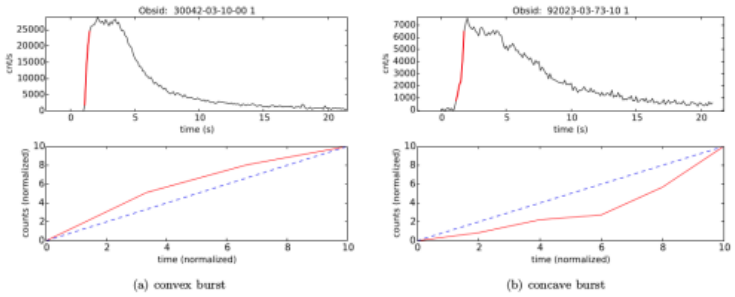

Figure 1: An example of a convex burst (a) and a concave burst (b). Taken from Figure 6 in Zhang et al. (2016). The top panels show two burst profiles, observed by the RXTE's PCA, the rising section of the burst is highlighted in red. The bottom panels show the normalised profiles of the highlighted sections. The convexity is the integrated area above or below the horizontal green dashed line in the plots. Area above the line is considered positive, and area below the line is considered negative.

1.d.3. Rising Time

The rising time of a burst, measured in seconds, is defined as the time it takes for the burst to reach its peak flux, measured from its start time, the start time of the bursts in this thesis was defined as the point where the flux of the burst reaches over 10 percent of the flux at the peak of the burst.

1.d.4. Fluence

The fluence is the time integrated flux received from a source. To integrate over the time period of a burst we use our initial time that was used in calculating the rising time. We also need to have an end time for the bursts, for each burst this end time was defined as the point where 90 percent of the energy of the burst had been dissipated (Ming Lyu et al. 2016).
In the case of an approximated blackbody the bolometric fluence is thus related to the flux as follows:

$$E_{\mathrm{b}} = \int_{t_i}^{t_e} F_{\mathrm{b}}(t)\,\mathrm{d}t, \tag{2}$$

where E_b represents the fluence, measured in erg cm^{-2}, F_b is the blackbody (bolometric) flux and t_i and t_e represent the initial time and end time of the burst, respectively.

1.d.5. Duration

The duration of the burst is a characteristic timescale, it gives us an impression of the length of the burst, it is related to the fluence and peak flux as follows:

$$\tau = \frac{E_b}{F_{peak}}, \tag{3}$$

The duration is denoted by τ and is measured in units of seconds.

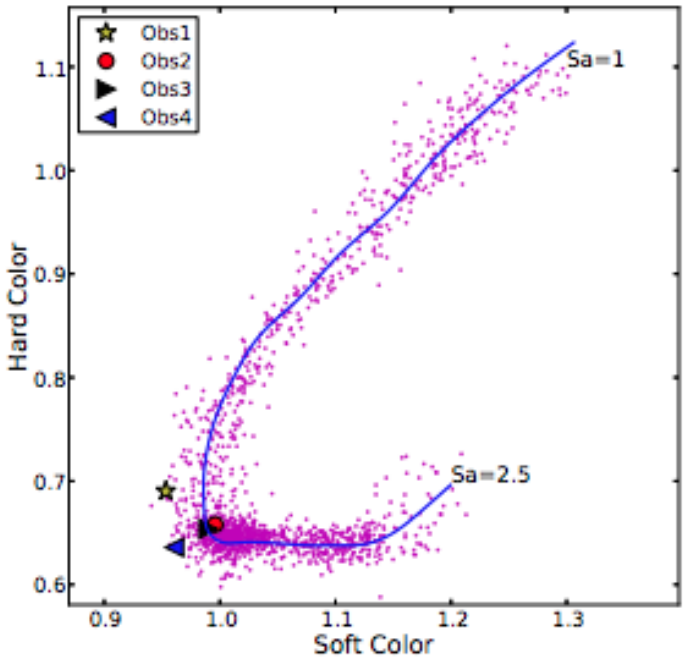

Figure 2: Color-color diagram of 4U 1636-53 taken from Ming Lyu et al (2016). The magenta points represent the averaged Crab-normalised colors (for more information see Zhang et al, 2011) of a single RXTE observation. Obs1-4 are four bursts observed by the RXTE that are also present in the data used in this thesis. They are placed in the figure at the point corresponding to the emission of the source just prior to the burst. Here hard and soft color are defined as the $(9.7-16.0)/(6.0-9.7)$ keV and the $(3.5-6.0)/(2.0-3.5)$ keV count rate ratios, respectively. The position of the source in the diagram is parameterised by the blue horseshoe shaped curve, this curve corresponds to values for the coefficient S_a. When an LMXB source emits high in hard color, it is termed as being in the hard state. If a burst happens while the source is in this state it will be placed at the top of the horseshoe curve. the transitional state refers to the point where, relatively speaking, the proportions of hard and soft color are more equal, which corresponds to the middle of the horseshoe shape. Finally, when a source emits more soft color, this source is positioned at the other end of the horseshoe, the source is then termed as being in the soft state.

1.e. Color-color diagram

Color−color diagrams are a means of comparing the relative intensities of sources over different wavelength regimes. In astronomy we typically observe a source over a narrow band around a wavelength, the intensity of an object observed will vary greatly across different wavelength regimes, and thus the objects will have different brightnesses in each band. In astronomy the ratio of intensities for two bands is referred to as color. On a color-color diagram, as one would expect, colors are plotted against one another. A color defined by the ratio of intensity in two wavelength bands is plotted on the horizontal axis, and then, on the vertical axis, another color defined over two different bands (or perhaps one band is used in determining both colors) will be plotted. Each X-ray burst from an LMXB can be plotted on a color-color diagram, in accordance with the state of the source immediately prior to the burst, as seen in figure 2.

1.e.1. S_a

S_a is a dimensionless coefficient that can be associated with a burst, it was initially formulated as an adapted version of the the S_Z parameterization (e.g., Wijnands et al. 1997b), but adapted for atoll sources. Originally formulated in this manner by Méndez, M (1999), S_a is used to measure positions along a spline that approximates the evolution of a source across a color-color diagram. An example of this parameter is given in figure 2. For atoll sources, S_a increases along the track of the color-color diagram, and it is thought that mass accretion rate increases monotonically with S_a (Hasinger & van der Klis 1989; Zhang et al. 2011).

1.f. mHz QPO

Close to half of the neutron star accretors in low mass X-ray binaries show Type-1 X-Ray bursts (e.g, in't Zand et al. 2004; Liu et al. 2007; Galloway et al. 2008). These bursts are due to the unstable thermonuclear burning of accumulated hydrogen and helium on the surface of a neutron star (e.g. Fujimoto et al. 1981). In recent decades another observational phenomenon related to nuclear burning on the surface of neutron stars has been uncovered. This phenomenon is termed a quasi periodic oscillation (QPO), it is theorised to be caused by a mode of burning on the surface of neutron stars that is in between stable and unstable burning, and is thusly termed 'Marginally Stable' burning. A subset of quasi-periodic oscillations (QPOs) which occur at frequencies of a few mHz were first detected by Revnivtsev et al. (2001) in three neutron star low-mass X-ray binaries (NS LMXBs), 4U 1608-52, 4U 1636-53, and Aql X-1. These QPOs spanned a low frequency range (7-9 mHz) and showed strong flux variation at photon energies of around (<5Kev). These two features were significantly aberrant compared to other QPOs in NS LMXBs, such as the kilohertz (kHz) QPOs recorded in various other studies (see e.g. van der Klis 2000, 2006; Méndez 2000, 2006; Méndez, van der Klis & Ford 2001; Belloni, Méndez & Homan 2005; Jonker, Méndez & van der Klis 2005; Linares et al. 2005; Boutloukos et al. 2006; Altamirano et al. 2008c; Sanna et al. 2010) and low-frequency QPOs (see e.g. Psaltis, Belloni & van der Klis 1999; Wijnands & van der Klis 1999; Belloni, Psaltis & van der Klis 2002; van Straaten et al. 2002; van Straaten, van der Klis & Méndez 2003; van der Klis 2004; Altamirano et al. 2005, 2008b, 2012). It was observed that mHz QPOs only appear when the source emits over a particular range of X-ray luminosities, this range was documented as $L_{220keV} \approx (5-11) \times 10^{36}$ erg s^{-1} (Revnivtsev et al. 2001; Altamirano et al. 2008a) and furthermore, the mHz QPOs are stronger at photon energies lower than 5 keV (Revnivtsev et al. 2001; Altamirano et al. 2008). Linares et al (2010) uncovered mHz QPOs in the neutron star transient IGR J17480-2446 based in the globular cluster Terzan 5. These particular mHz QPOs displayed different properties compared to previously observed mHz QPOs. Their QPO frequency was below 4.5 mHz, outside of the typical range of Revnivtsev et al. (7-9 mHz). The source luminosity at the time that these QPOs appeared was also rather high ($L_{2-50keV} \approx 10^{38}$ erg s^{-1}). A few years later, Linares et al. (2012) found a case of smooth evolution between X-ray bursts and mHz QPOs in IGR J17480-2446, during which the luminosity of the source changed during the outburst, this had never been observed in another mHz QPO source.

These differences between a conventional QPO and a mHz QPO suggested that the mechanism that is responsible for their generation is different (e.g, van Straaten et al. 2002, 2005; van der Klis 2006, Altamirano et al. 2008) in NS LMXBs. Revnivtsev et al. (2001) proposed that the mHz QPOs were generated via a unique mode of nuclear burning on the neutron star surface; it was further posited that this mode of burning only occurs within a certain range of mass accretion rates. It was proposed by Heger, Cumming & Woosley (2007) that mHz QPOs are due to the marginally stable nuclear burning of helium at the surface of neutron star accretors. The oscillation's characteristic timescale using the Heger model is similar to the characteristic time scale of around 2 minutes that is seen in mHz QPOs in NS LMXBs, lending credence to this theory. Another prediction that the Heger model makes is that the QPOs should occur in a narrow range of X-ray luminosities, matching what was previously observed. The one flaw in the Heger model

is that the accretion rate at which the mHz QPOs were predicted is close to the Eddington rate, which is one order of magnitude greater than the rate that can be inferred from the X-ray luminosities at which mHz QPOs have been observed previously. To explain this disparity it was put forth that perhaps, the local accretion rate at the burning depth can be higher than the global accretion rate, this would mean that the posited relation between accretion rate and QPOs observed in the mHz frequency range would still be plausible, and the model of Heger et al. (2007) would still be valid. Keek et al. (2009) discovered that turbulent chemical mixing as well as a higher heat flux on the crust of a neutron star can explain the observed accretion rates at which mHz QPOs are seen. Keek et al. (2014) explored the effect of fuel composition and nuclear reaction rates on the mHz QPOs. It was concluded that no permissible variation in the composition and reaction rate is able to trigger a mHz QPO at the observed accretion rates.

Lyu et al. (2015) studied the relation between the frequency of the mHz QPOs and the temperature of the neutron star surface in the NS LMXB system 4U 1636-53 using simultaneous XMM-Newton and RXTE observations. It was discovered that there was no significant correlation, which did not fit with previous theoretical predictions. On top of this, Lyu et al. (2015) also found that all seven X-ray bursts that were associated with mHz QPOs in this source were bright, energetic and short, this indicated a potential link between the mHz QPOs and helium rich X-ray bursts.

Maurer & Watts (2008) simulated the influence of ignition latitude, neutron star rotation and accretion rate on the profile of the rising phase of type 1 X-ray bursts, they discovered that bursts which ignite on the equator will always have positive convexity, whereas bursts that ignite at high latitude could possibly have positive or negative convexity. Mahmoodifar & Strohmayer (2015) confirmed that the rising section of the light curve of an X-ray burst is more concave when ignition begins near the poles compared to when it starts near the equator of a neutron star. Therefore it can be said that the convexity of an X-ray burst provides information about the ignition site of unstable nuclear burning on the neutron star surface.

From this evidence it is clear that mHz QPOs are connected to type 1 X-ray bursts, it is possible to study the origin and underlying physics of marginally stable nuclear burning on the surface of an accreting neutron star by investigating the mHz QPOs and type 1 X-ray bursts together. In this thesis, similar to the research done by Lyu et al. (2015), I will study mHz QPOs associated with type 1 X-ray bursts in 4U-1636-53.

1.g. RXTE satellite

The Rossi X-Ray Timing Explorer was launched on December 30, 1995, at Cape Canaveral via a Delta rocket launcher. The rocket followed a circular, low-earth orbit at an altitude of 580km, these orbital parameters correspond to an orbital period of approximately 96 minutes. The RXTE was initially slated to operate for a span of two to five years. The mission, however, surpassed its expectations and actively carried out observations for 16 years before finally being decommissioned on the 5th of January, 2012. The RXTE was designed to observe extreme environments such as those associated with white dwarfs, neutron stars and black holes. The RXTE possessed three different instruments, the All-Sky Monitor, the Proportional Counter Array and the High-Energy X-ray Timing Experiment. The ASM was capable of observing over 80 percent of the sky during each orbit, under a spatial resolution of 3' x 15'. The ASM itself was made up of three Scanning Shadow Cameras, each possessed a field of few of $6^\circ \times 9^\circ$ and an effective area of approximately 30 cm^2. This instrument was sensitive to energies in the 1.5-12 keV energy range and functioned with a time resolution of 0.125 seconds [25]. The primary use of the ASM was producing long term X-ray light curves for bright, persistent X-ray sources. The ASM was also useful in the detecting new outbursts or transients. The main instrument mounted on the RXTE was, however, the PCA. The PCA consisted of five identical proportional counter units (PCUs). Each PCU was sensitive to the energy range of 2-60 keV, and altogether had a combined effective area of around 6500 cm^2. The PCA had a time resolution of around 1 μs and an energy resolution of around 1 keV at 6 keV [25]. The combination of having a large effective area and a relatively high time resolution made

the PCA particularly well suited for studies into timing variability. The remaining instrument on board, the HEXTE, was comprised of two clusters of detectors, each cluster was made up of four scintillation detectors which were sensitive to photos in the energy range of 15-250 keV, each cluster was collimated to view a 1° field. The total effective collecting area of both clusters was 1600 cm^2. HEXTE possessed a time resolution of 8μs and an energy resolution of around 10 keV at 60 keV. [25]

The light curves that underwent statistical analysis in this thesis were obtained only through observations undertaken by the PCA.

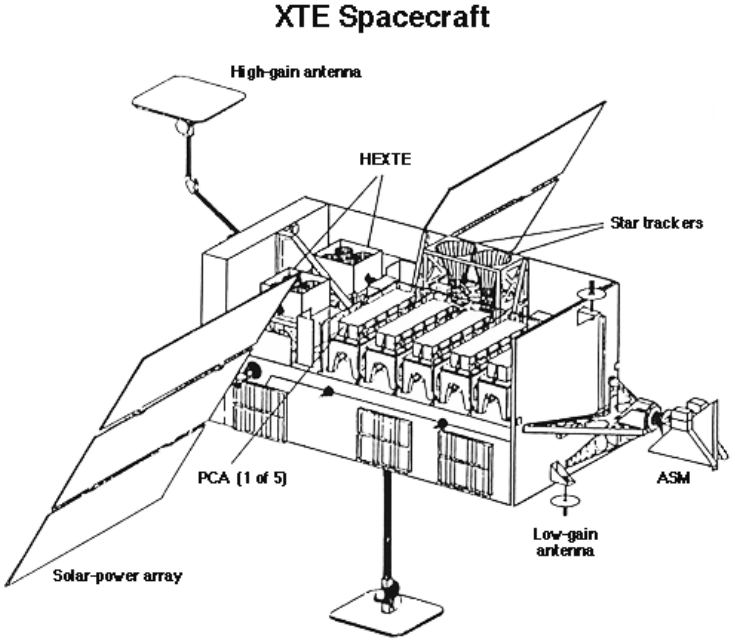

Figure 3: Diagram of the RXTE spacecraft and its instruments. Taken from [5] `https://heasarc.gsfc.nasa.gov/Images/xte/xte_spacecraft.gif`

2. Observations and Data analysis

The data of object 4U 1636-53 that was to be analysed came from the PCA (Jahoda et al. 2006) which was situated on board the RXTE satellite. An observation with the RXTE normally covers 1 to 5 consecutive 90 minute orbits. An orbital observation contains between 1 and 5 ks of useful data, separated by 1-4 ks data gaps. On rare occasions the visibility windows aligned so that it was possible for the RXTE to continuously observe the source for up to 27 ks. The data set analysed in this thesis therefore consists of continuous data segments ranging in length between 0.3-27 ks.

2.a. Finding mHz QPOs in the RXTE data

In previous work by (Ming Lyu, Guobao Zhang, Méndez et al. (2016)) 1-s resolution event mode PCA light curves were used at around the 2-5 keV range to find mHz QPOs (this was previously found to be the range where mHz QPOs are of the largest magnitude, Altamirano et al. 2008). The periodicities in each of the gap-free segments were searched for separately using Lomb-Scargle periodograms (Scargle 1982). In cases where more than one type 1 X-ray burst was detected, a mHz QPO was searched for before, after and in between bursts. The mHz QPOs were only detected when they reached a minimum 3σ significance as outlined in the method used in Press et al. (2002). When undetected, it was hard to estimate a meaningful upper limit on the fractional rms amplitude of the mHz QPOs before an X-ray burst. This was due to issues such as: data-gaps immediately prior to the burst, the segment before the burst being too short to properly discern a QPO, or possibly that there were a reduced number of PCUs active during that certain observation. In cases where the aforementioned problems were not present, 3σ upper limits as low as 0.4% rms were estimated for the 2-5 keV range.

2.b. Finding bursts in the RXTE data

Light curves were produced from the standard-1/Event data that spanned 0.25 seconds [25], and these light curves were scanned for bursts using the methodology described in Zhang et al. (2011). In order to study the shape and time-scale of the bursts initial rise, the light curves from the PCA data with 0.125-s time resolution were extracted. To describe the shape of the bursts rising phase quantitatively, the parameter C, known as convexity, was used in the analysis (Maurer and Watts 2008). The method of Maurer and Watts (2008) was then applied to calculate the convexity in the burst light curves for the full PCA energy band; for more details on these phases of data reduction refer to Zhang et al. (2011). The rising time of each burst, defined as the time interval during which the flux in the light curve is between 10 and 90 percent of the flux at the peak of the burst.

In the entire RXTE archive there were a total of 371 X-ray bursts originating from the source 4U 1636-53 that had been recorded. In previous work carried out by Guobao Zhang et al. (2011) this set of 371 bursts were further refined by exempting bursts that showed at least one of the following characteristics: (i) The rise up to the peak of the burst's light curve was incomplete, (ii) The burst's light curve possessed multiple peaks, and the first peak was not the highest, (iii) the burst was itself of a low intensity and thus was hard to be adequately discerned due to background noise. Finally, a superburst contained in this dataset (Wijnlands 2001) was also excluded. After making the aforementioned exemptions the remaining 305 X-ray bursts all possessed a complete smooth profile.

2.c. Associating the mHz QPOs with the bursts

In the RXTE archive of 4U 1636-53 observations there were 168 cases of mHz QPOs detected. In further work carried out by Guobao Zhang et al. (2011) these mHz QPOs were associated to bursts from the set of X-ray bursts previously discussed. An X-ray burst and mHz QPO were considered associated if, during an observation, there was a mHz QPO that ended at the same time as an X-ray burst began. Out of the total 305 X-ray bursts it was found that 39 were associated

with a mHz QPO. The mHz QPOs in these observations always disappeared at the time when the associated X-ray burst began.

2.d. Spectral and timing techniques

LMXBs normally emit over a large energy range, from radio wavelengths up to the gamma-ray band. These emissions provide plenty of information with regards to the physical processes occurring in the system. In the X-ray band, with the resolution of current telescopes and the average distances to these objects being as they are, it is rather difficult to attain significant information directly from the images observed by a telescope. To circumvent this problem spectroscopic and timing analysis techniques are used. These techniques help us study the physical mechanisms that are active inside LMXBs. In LMXBs different emitting regions, such as the accretion disc or corona, generate radiation via different mechanisms. The components from each region combined with each other form the whole energy spectrum that is observed. If studying the individual components is desired, it is necessary to fit the whole energy spectrum so that the components can be separated. Different theoretical models are used to describe different components and a chi-square test is usually applied to test whether the resulting fit is adequate. One flaw of these methods is that the results from these methods of spectral analysis are heavily dependent on the models that are selected. In previous work carried out by Ming Lyu et al. (2016) the spectra of all bursts in 4U 1636-53 were analysed using XSPEC version 12.8.0 (Arnaud 1996). The spectral fits were restricted to the energy range 3.0 - 20.0 keV, and the time resolved spectra were fitted to a single temperature blackbody model (Named BBODYRAD in XSPEC) multiplied by a component that accounted for interstellar extinction towards the source. The intervening hydrogen column density N_H was assumed constant and fixed at 0.36×10^{22}, in accordance with (Sanna et al. 2013). The spectral model provided two free parameters: blackbody color temperature and normalisation, which is proportional to the square of the blackbody radius of the emitting surface, this allows an estimate of the bolometric flux during the burst. The burst fluence E_b values for each burst are the flux values integrated over the burst time period. For further details into the spectral and timing techniques used to attain the flux values for the bursts used in this thesis, refer to Ming Lyu et al. (2016).

2.e. Uncertainty

2.e.1. Flux

Ming Lyu et al. (2016) created spectral models to find the blackbody temperature T_b and blackbody normalisation N_b of each burst. From these models uncertainty margins for these respective quantities were attained. The equation for flux received from a blackbody at a given distance from a source, is an adapted form of equation (1), and it follows the relation:

$$F_b = \frac{\sigma T_b^4 R^2}{d^2}, \tag{4}$$

where the variables R and d represent the radius of the emitting source, and d the distance to the source. By encompassing several of these variables in the normalisation N_b and A, it is possible to rewrite this equation as:

$$F_b = A N_b (k T_b)^4, \tag{5}$$

where A is a constant, and k is the Boltzmann constant.

Uncertainty propagation laws give us an equation for the error in our flux, and after simplification superfluous elements, such as the constant A, fall out, we therefore see that the uncertainty in flux follows the simplified equation:

$$\frac{\sigma_{F_b}^2}{F_b^2} = \frac{\sigma_{N_b}^2}{N_b^2} + 16\frac{\sigma_{kT_b}^2}{{kT_b}^2}, \tag{6}$$

where $\sigma_{F_b}, \sigma_{N_b}$ and σ_{kT_b} represent the uncertainties in the flux, normalisation and kT_b, respectively.

Once I calculated all the flux uncertainties for a subset of 71 of bursts, I gathered the max flux uncertainty values that were attained for each separate burst - as the maximum uncertainty values will correspond to the peak of the fluxes - and then calculated the median of the values over the entire 71-burst range. This median uncertainty value of $\pm 1.46 \times 10^{-8}$ erg cm^{-2} s^{-1} I took to represent the characteristic error in the peak flux ($\sigma_{F_{peak}}$) for all 305 bursts. The use of a characteristic error was to prevent clutter in the figures and still give the reader of this thesis an idea of the characteristic uncertainties in the measurements.

2.e.2. Fluence

The characteristic uncertainty in the fluence can be found via the relation:

$$\sigma_{E_b} = \sqrt{\delta t^2 \sum \sigma_{F_b}^2}, \tag{7}$$

In this case I took σ_{F_b} to be the mean of the uncertainties over the same subset of 71 bursts, as this would yield values closer to the true values for σ_{E_b}, the fluence uncertainty, this is because fluence is calculated via an integral over the full range of fluxes. δt here represents the time interval used in the flux observations, this was always less than 0.5 seconds and so I use this upper limit on δt as the time uncertainty. I also used this value as the uncertainty in the rising time. We yield a final characteristic uncertainty value for σ_{E_b} of $\pm$ 5.61 $\times$ 10^{-8} erg cm^2.

2.e.3. Duration

The final characteristic uncertainty to be calculated was that of the duration, τ, this uncertainty can be calculated from the uncertainties for fluence and peak flux yielded earlier. The relation between these is as follows:

$$\sigma_\tau = \tau \times \sqrt{((\frac{\sigma_{E_b}}{E_b})^2 + (\frac{\sigma_{F_{peak}}}{F_{peak}})^2)}, \tag{8}$$

The uncertainty in duration, σ_τ (seconds), was thus calculated for each duration value for all 305 bursts. The mean value of these was then used as the characteristic uncertainty in duration. Out final value for duration uncertainty was found to be $\pm$6.34 seconds.

The characteristic uncertainty values derived in this section are roughly of the same magnitude as the true uncertainty in the measurements, and thus provide insight into our observations.

2.e.4. Convexity and color

The convexity and color uncertainties were not explicitly derived in this work. For more information on the calculation of convexity for the bursts see Zhang et al. (2016). For more information on the color uncertainties see Lyu et al. (2016).

3. Results

For brevity's sake, I will henceforth refer to the bursts that are not associated with a mHz QPO as 'plain' bursts, and those that are as mHz QPO bursts.

In figure 4 the values of hard and soft color for the bursts were plotted against each other on a color-color diagram. Hard and Soft color values were defined as the $(9.7-16.0)/(6.0-9.7)$ keV and $(3.5-6.0)/(2.0-3.5)$ keV count rate ratios. I used the parameter S_a to indicate the approximate location of the source in the color-color diagram (Méndez & van der Klis 1999; Zhang et al. 2011). The parameter S_a was thus defined such that $S_a = 1$ corresponded to the top right vertex of the diagram and $S_a = 2$ to the bottom left vertex. I also plotted the rough curve that was used to define the S_a values of each observation. The blue dots represent the sources color-color state just before a plain X-ray burst, and the red dots represent the source's state prior to one of the 39 mHz QPO bursts. The rough line along the diagram represents the parameterisation of the S_a values. It was found that all mHz QPO bursts were clustered around the lower left of the curve. The S_a values of the entire dataset ranged from 1.07 to 2.45, however the 39 mHz QPO bursts had S_a value ranging from 1.78 to 2.38 with a mean value of 2.06 and a standard deviation of 0.13. These values of S_a imply that the mHz QPO bursts appeared around the transitional spectral state. The fact that the mHz QPO bursts cluster around one section of the color-color diagram, at a rather high value of S_a, also implies that they originate from regions that possess a higher mass accretion rate (Hasinger & van der Klis 1989; Zhang et al. 2011).

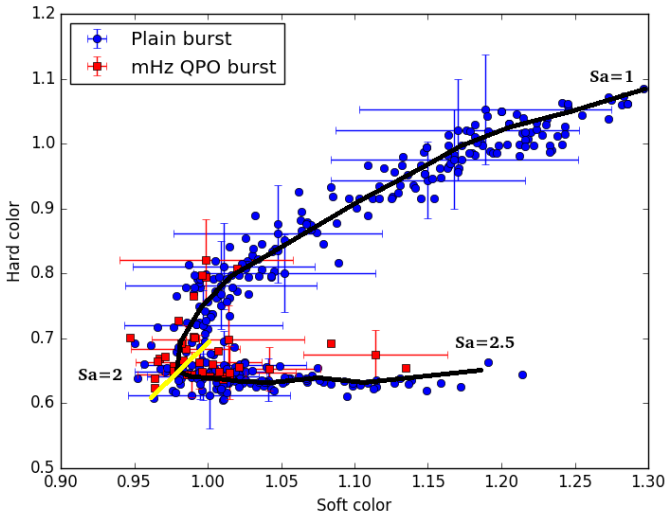

Figure 4: Color-color figure of 4U 1636-53, here the black curve is a rough demonstration of the path of the coefficient S_a, the yellow line at the middle of the curve represents a value of around $S_a = 2$. Error bars have not been added to every point to prevent clutter.

In figure 5 the 39 bursts associated with a mHz QPO have once again been marked with red squares, whereas the remaining 266 bursts have been marked with blue circles. Figure 5 shows the values of peak flux, convexity, rise time, fluence and duration for these two subsets of bursts, plotted against their value of S_a.

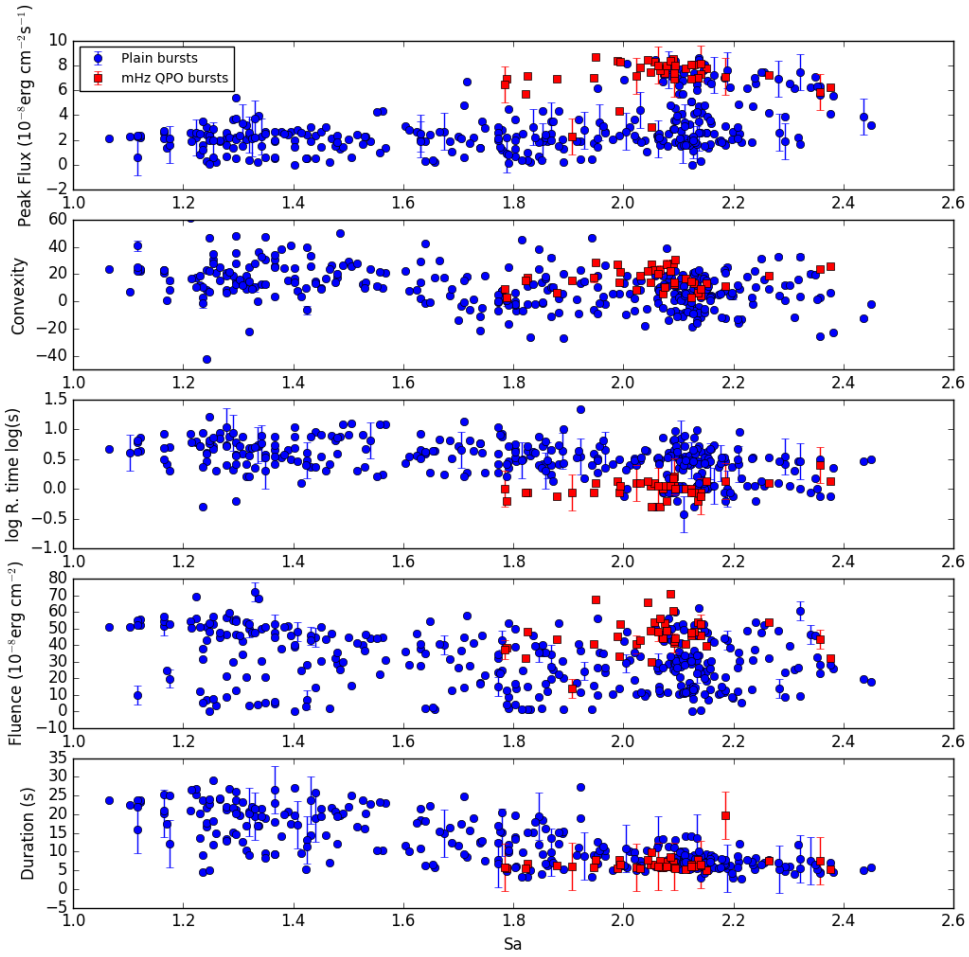

Figure 5: Several properties of X-ray bursts in 4U 1636-53 plotted against S_a. Error bars have not been added to every point to prevent clutter.

In figure 5 we can see the rough distribution of peak fluxes, the values range from close to 0 to 8.65×10^{-8}erg cm^{-2} s^{-1}, with a mean value of 3.40×10^{-8} and a standard deviation of 2.35×10^{-8}. For the subset of the bursts that were associated with a mHz QPO the range of peak flux values differed significantly. For these 39 mHz QPO bursts the values of peak flux ranged from 2.30×10^{-8} to 8.65×10^{-8} erg cm^{-2} s^{-1}, and they possessed a mean value and standard deviation of 7.17×10^{-8} and 1.36×10^{-8} erg cm-2 s^{-1}, respectively. It appears that the peak fluxes of the plain bursts seem to follow a bi-modal distribution, this is more clearly evident in figure 6, a histogram showing the distribution of the peak flux values attained by the mHz QPO bursts in red, and those attained by the 'plain' bursts in blue. We can see the distribution of the plain bursts possesses two centres around 2.5×10^{-8} and 7×10^{-8} erg cm-2 s^{-1}. Analysing the peak fluxes of the 39 mHz QPO bursts, it is seen that 36 out of the 39 mHz QPO bursts have a flux above 5×10^{-8} erg cm-2 s^{-1}, which is much higher than the average peak flux for the remaining 266 bursts. Furthermore, I performed a Kolmogorov-Smirnov (KS) test on the peak flux distribution of the mHz QPO bursts, testing them against the larger dataset of the plain bursts. My KS test yielded a null hypothesis probability of 1.21×10^{-19}, this is low enough that we can consider it conclusive evidence that the plain bursts and the mHz QPO bursts peak fluxes come from two different parents distributions. I conclude that the presence of a mHz QPO is connected to the peak flux of a burst, and that bursts associated with a mHz QPO are more energetic than plain bursts.

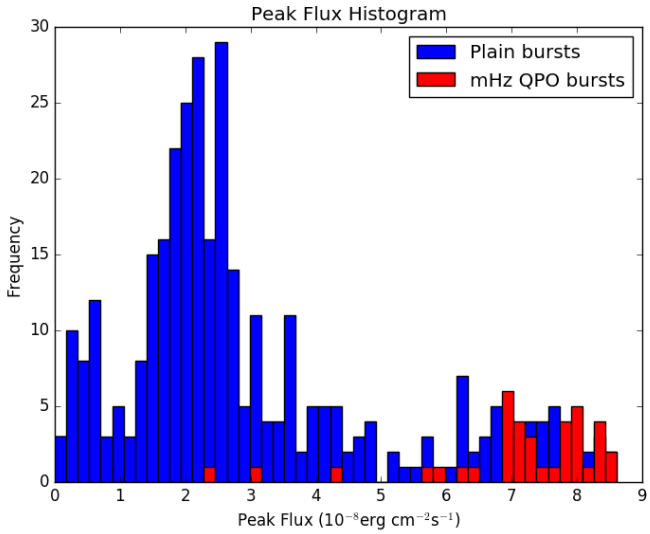

Figure 6: Histogram showing the distribution of peak flux for both subsets of X-ray bursts in 4U 1636-53.

The convexity of all the bursts range from -42.2 to 61.3, with a mean value for all the bursts of 10.9 and a standard deviation of 14.3. I performed a KS test on the convexity distribution of the plain bursts against that of the mHz QPO bursts. The result of the KS test yielded a probability that they belong to the same parent distribution of 0.0018. This value implies that the plain bursts and mHz QPO bursts have different convexity distributions.

Ming Lyu et al. (2016) also conducted analysis on the convexities of the 305 bursts from 4U 1636-53, it was discovered that the distribution of the convexities was symmetric. 252 of the bursts showed positive convexity, and 53 showed negative convexity. The overall distribution of convexities could be fitted with a Gaussian function (yielding a coefficient of determination = 0.976) with a mean value of 12.3 $\pm$ 1.2, to a confidence level of 95 percent, and a standard deviation of 12.6 $\pm$ 1.2. All 39 mHz QPO bursts were found to have positive convexity. The range of values for the mHz QPO bursts was 2.63 to 31.02. The probability P_{39} of selecting 39 bursts from the aforementioned Gaussian distribution and yielding 39 bursts with only positive convexity (figure 7) can be estimated by the binomial distribution, since the bursts can be positive or negative. The probability of a selecting a positive burst is then $252/305 = 0.826$. The probability of selecting 39 bursts with positive convexity is then $P_{39} = 0.826^{39} = 5.6 \times 10^{-4}$.
Both these results imply that the presence of a mHz QPO is related to the convexity of the associated burst.

The rising time of all bursts were found to roughly follow a bi-modal distribution (see figure 8), with peaks at 1 second and 3 seconds, respectively. The mHz QPO bursts were all found to be quite short compared to the plain bursts. The rise times of the mHz QPO bursts range from 0.5 to 2.5. We can see from the histogram, figure 7, that the mHz QPO bursts mostly fall around the first peak of the bi-modal distribution. All these mHz QPO bursts have a rising time below 2 seconds, with only one exception, and the mean value of all mHz QPO bursts was 1.07 seconds, with a standard deviation of 0.36 seconds. I performed a KS test to see how likely it was that the two datasets (plain and mHz QPO bursts) are from the same parent distribution. The KS test yielded a probability value for this null hypothesis of 7×10^{-21}, which is very low - enough to discount this null hypothesis. I conclude that the presence of a mHz QPO is connected to the rising time of the associated burst, and that bursts associated with a mHz QPO are shorter than plain bursts.

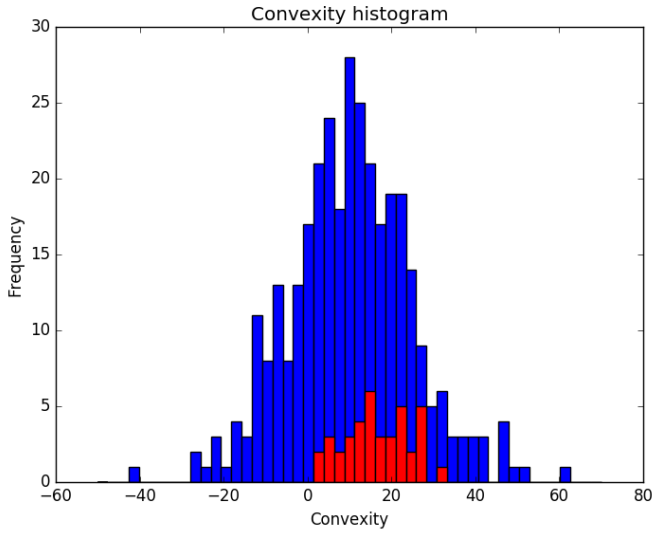

Figure 7: Histogram of the convexity distributions of both subsets of bursts in 4U 1636-53. The plain bursts bars are blue, and the mHz QPO bursts bars are colored red.

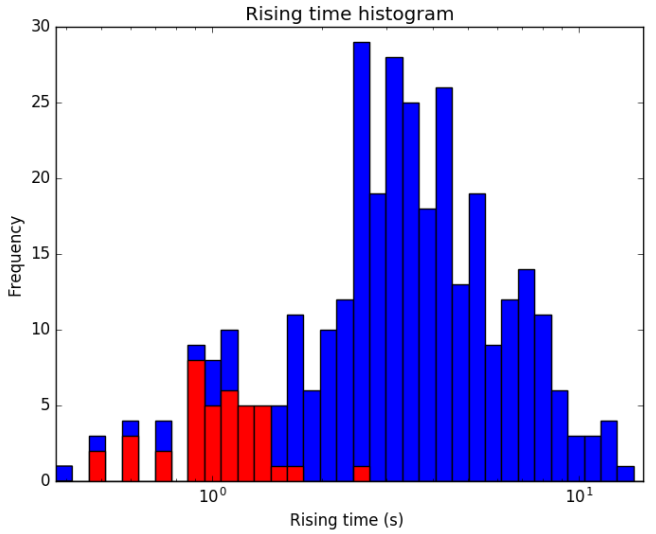

Figure 8: Histogram showing the distribution of rising time for both subsets of the bursts in 4U 1636-53. the plain bursts bars are blue, and the mHz QPO bursts bars are colored red.

The fluence values, measured in units of 10^{-8} erg cm^2, of all the bursts range from 0.01 to 140.3, with a mean value of 32.7 and a standard deviation of 18.2. For the 39 bursts associated with a QPO we see the values range from 14.0 to 140.3 with a mean value of 48.4 and a standard deviation of 18.3. I conclude that the fluence values of the mHz QPO bursts are significantly higher than that of the plain bursts. I plotted the the distribution of burst fluence values as a histogram (figure 9), with the 39 bursts mHz QPO bursts in red, and the remaining bursts colored in blue. We see that the bursts associated with a mHz QPO are distributed differently than the plain bursts, this is corroborated by a KS test on the two datasets which yielded a value of 3.55×10^{-8}. A number this low suggests the mHz QPO bursts and the plain bursts belong to two different parent distributions.

The duration of all bursts ranges from 2.85 to 28.97 seconds. With a mean value of 11.51 and

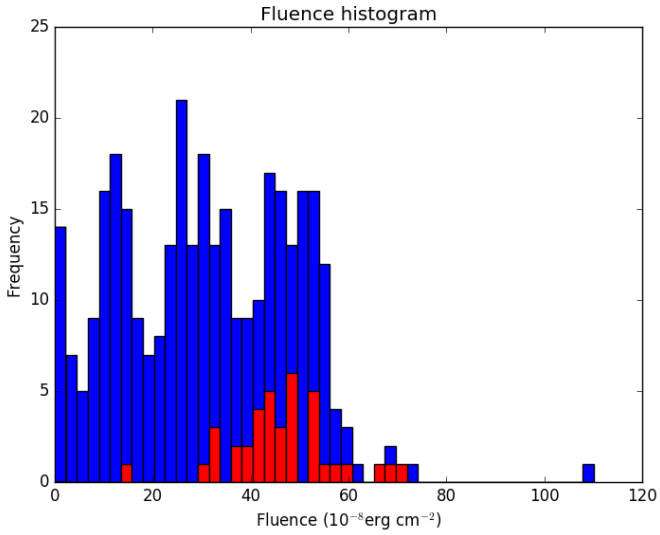

Figure 9: Histogram of fluence distribution of both subsets of X-ray bursts in 4U 1636-53. the plain bursts bars are colored blue, and the mHz QPO bursts bars are colored red.

a standard deviation of 6.42. For the bursts associated with a QPO the duration range is from 5.08 to 19.76 seconds. The mean and standard deviation for the QPO bursts is 6.80 and 2.33, respectively. The disparity in duration for the mHz QPO bursts and the plain bursts is further illustrated in the histogram, figure 10. I performed a KS test to identify the likelihood of whether these two datasets originate from the same parent distribution. The KS test yielded a value of 1.80×10^{-9}. A value this low suggests that we can reject this null hypothesis. This result shows that mHz QPO bursts have a shorter duration than plain bursts.

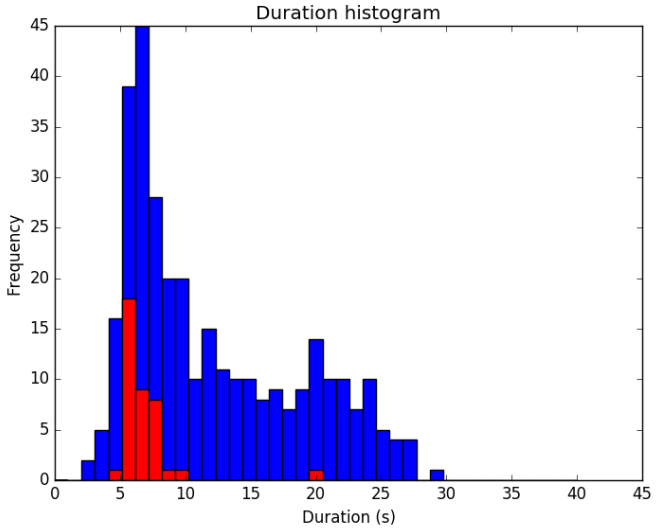

Figure 10: Histogram of duration distribution for both subsets of bursts in 4U 1636-53, the plain bursts bars are blue, and the mHz QPO bursts are colored red.

4. Discussion

I conclude, similarly to Lyu et al.(2016), that there is a connection between mHz QPOs and the properties of an associated type 1 X-ray burst. From our statistical analysis I gathered that the bursts associated with a mHz QPO, and those that are not, come from two different parent populations. Firstly, the S_a values of the 39 bursts associated with a mHz QPO were all clustered around a mean value of 2.06 with a standard deviation of 0.13, a very different range compared to the plain bursts. It can also be inferred from this that the mHz QPO bursts occurred almost always around the transitional state. A high value of S_a is thought to correspond to an increased value of the mass accretion rate, laying credence to the model of mHz QPOs made by Heger et al. (2007).

The bursts associated with a mHz QPO also had further noticeable differences with respect to their properties compared to the plain bursts. They were almost always very energetic and possessed a short duration, and thus, high fluence. They also showed a very short rising time compared to the plain bursts. KS testing the 39 mHz QPO burst's fluence, rising time, duration and peak flux, against those of the plain bursts, I found that the probability that the bursts came from the same parent distribution, with regards to each of the aforementioned properties, was very unlikely. (Fujimoto et al. 1981; Narayan & Heyl 2003) Showed how the differences in rise and decay timescales can generally be well explained by differences in rates of mass accretion, as well as the chemical composition of the neutron star's surface in an NS LMXB. It was theorised that at low mass accretion rates the low temperature in the burning layer means the accreted hydrogen burns unstably and produces bursts that are more rich in hydrogen, with a slow rise and decay. Galloway et al. (2008) further backed this claim that protracted bursts, with a slow decay and rising time were likely to be fueled by a mix of hydrogen and helium, whereas faster bursts with shorter rising time were found to likely have a fuel rich solely in helium. This is because hydrogen burning proceeds slower than helium burning as it relies on β-decay which is moderated by the weak nuclear force. At higher accretion rates the hydrogen burns into helium during accretion, this builds a layer of helium on the NS surface. Once the fuel layer has heated sufficiently helium ignition occurs. Since this burning process is mediated via the triple-α process it is very unstable, hence helium bursts show fast rising and decay time. From this prior research I conclude that the bursts associated with a mHz QPO are the result of the burning of a helium rich fuel.

The convexities of the 39 mHz QPO bursts were all found to be positive, the probability of this occurring if the mHz QPO burst's convexities were from the same parent distribution as the plain burst's is very small according to my KS testing, and the gaussian fitting of Lyu et al. (2016). Maurer & Watts (2008) used simulations to map the propagation of a burning front on the surface of a neutron star. They found that bursts that ignite at the equator will always have a positive convexity, whereas those that ignite at a high latitude could possess either positive or negative convexity. Mahmoodifar & Strohmayer (2015) strengthened this result with their own simulations. In addition they found that when bursts ignite at the equator their rising times tend to be shorter, whereas those that ignite at higher latitudes could possess short or long rising times. Based on these previous studies I propose that the 39 mHz QPO bursts ignited at the neutron star equator. When a neutron star accretes matter from a donor, the matter first reaches the equator, before spreading over the entire surface of the neutron star, the local accretion rate will therefore be higher at the equator (Lyu et al. 2016). This situation bridges the disparity between the high mass acretion rates necessary for mHz QPOs in the model of Heger (2007) and the observed accretion rates in NS LMXBs.

References

[1] Altamirano D. Van der Klis M., Wijnans R., Cumming A., 2008 ApJ, 673, L35

[2] Altamirano D., van der Klis M., Méndez M., Jonker P. G., Klein-Wolt M., Lewin W. H. G., 2008, ApJ, 685, 436

[3] Arnaud K. A., 1996, in Jacoby G. H, Barnes J. eds, Astronomical Data Analysis Software and Systems V VOl. 101 of Astronomical Society of the Pacific Conference Series, XSPEC: The First Ten Years. p. 17

[4] Duchêne[1,2] & Kraus[3]. 2013 (1) UC Berkeley , (2) Institut de Plantologie et d'Astrophysique de Grenoble, (3) Harvard-Smithsonian, Annual Review of Astronomy and Astrophysics, vol. 51:269-310, 10.1146/annurev-astro-081710-102602

[5] European Space Agency, 2018. retrieved from: https://www.cosmos.esa.int/web/cesar/x-ray-binaries-monitoring

[6] Fujimoto M. Y., Hanawa T., Miyaji S., 1981, ApJ, 247, 267

[7] Galloway D.J., Muno M. P., Hartman J. M., Psaltis D., Chakrabarty D. 2008, ApJS, 179 360

[8] Galloway D.K., Psaltis D., Muno M.P., Chakrabarty D. 2006 ApJ, 639, 1033

[9] Heger A., Cumming A., Woosley S. E., 2007 ApJ, 665, 1311

[10] Jahoda K., Markwardt C. B., Radeva Y., Rots A. H., Stark M. J., Swank J. H., Strohmayer T. E., Zhang W., 2006, ApJS, 163, 401

[11] Keek L., Langer N., int Zand J. J. M., 2009, A&A, 502, 871

[12] Keek L., Cyburt R. H., Heger A., 2014, ApJ, 787, 101

[13] Linares M., Altamirano D., Watts A., van der Klis M., Wijnands R., Homan J., Casella P., Patruno A., Armas-Padilla M., Cavecchi Y., Degenaar N., Kalamkar M., Kaur R., Yang Y., Rea N., 2010, The Astronomers Telegram, 2958, 1

[14] Linares M., Altamirano D., Chakrabarty D., Cumming A., Keek L., 2012, ApJ, 748, 82

[15] Lyu, M. (2016). Spectral and timing properties of neutron-star low-mass X-ray binaries, University of Groningen

[16] Mahmoodifar S., Strohmayer T., 2015, ArXiv e-prints

[17] Maurer I., Watts A. L., 2008, MNRAS, 383, 387

[18] M. Coleman Miller., Introduction to neutron stars, Date: N/A, University of Maryland. retrieved from: http://www.astro.umd.edu/~miller/nstar.html

[19] Méndez M., van der Klis M., Ford E. C., Wijnands R., van Paradijs J., 1999, ApJ, 511, L49

[20] Mitsuda K., Inoue H., Koyama K., Makishima K., Matsuoka M., Ogawara Y., Suzuki K., Tanaka Y., Shibazaki N., Hirano T., 1984, PASJ, 36, 741

[21] Revnivtsev M., Churazov E., Gilfanov M., Sunyaev R., 2001, A&A, 372, 138

[22] Robert Dunn, 2005. Black Holes and X-ray binaries. Published 1996-2009 by the Institute of Astronomy X-Ray Group. retrieved from: https://www.xray.ast.cam.ac.uk/xray_introduction/Blackholebinary.html

[23] Rothschild R. E., Blanco P. R., Gruber D. E., Heindl W. A., MacDonald D. R., Marsden D. C., Pelling M. R., Wayne L. R., Hink P. L., 1998, ApJ, 496, 538

[24] RXTE image gallery, 2012, NASA. retrieved from: https://heasarc.gsfc.nasa.gov/docs/xte/xte_1st.html

[25] RXTE GOF, Rossi X-Ray Timing Explorer (RXTE): December 1995 - January 2012, 2012, NASA. retrieved from: https://heasarc.gsfc.nasa.gov/Images/xte/xte_spacecraft.gif

[26] Sanna A., Hiemstra B., Méndez M., Altamirano D., Belloni T., Linares M., 2013, MNRAS, 432, 1144

[27] Scargle J. D., 1982, ApJ, 263, 835

[28] Sidika Merve Colak, Thermonuclear bursts, 2014
Dig Sites of Stellar Archeology: Giant Stars in the Milky Way Middle East Technical University. Ankara, Turkey, Special Issue, 2014, 173-178

[29] Sugimoto D., Ebisuzaki T., Hanawa T., 1984, PASJ, 36, 839

[30] van der Klis M., 2006, in Compact Stellar X-Ray Sources, ed. W. H. G. Lewin & M. van der Klis (Cambridge: Cambridge Univ. Press)

[31] van Straaten S., van der Klis M., di Salvo T., Belloni T., 2002, ApJ, 568, 912

[32] Wijnands R., 2001, ApJ, 554, L59

[33] Zhang G., Méndez M., Zamfir M., Cumming A., 2016, MNRAS, 455, 2004

[34] Zhang G., Méndez M., Altamirano D., 2011, MNRAS, 413, 1913